Nanoscale

PAPER

View Article Online
View Journal | View Issue

Cite this: *Nanoscale*, 2022, **14**, 16978

Highly-efficient radiative thermal rectifiers based on near-field gap variations†

Bei Yang [a,b] and Qing Dai *[a,b]

Near-field radiative thermal rectifiers (NFRTRs) enabling directional heat transport hold great promise for various applications, including thermal logic computing, thermal management, and energy conversion. Current NFRTR designs rely on dissimilar terminal materials with high contrasts in their temperature-dependent dielectric properties, which in turn hinders the spectral match for radiative heat transfer and thus limits the device's efficiency. Herein, this dilemma is solved by designing heterostructures where a pair of polaritonic layers are separately stacked on a thermally-expanding layer and a rigid substrate, spaced by a vacuum gap. In this scheme, the symmetric polaritonic layers can provide stable near-field radiative channels for heat transfer, while the thermally-expanding layer can modulate the gap size with flipped temperature bias to allow high contrasts in heat flux. In exemplified implementations, the hBN-based design has achieved a record-high thermal rectification factor (TRF, ~10^4) even under small thermal gradients (~20 K), which can be further boosted by polaritonic hybridizations in the graphene/hBN-based design. This study paves the way to design novel NFRTRs with 2D materials, thus providing enriched polaritons to realize higher TRFs.

Received 9th August 2022,
Accepted 19th October 2022

DOI: 10.1039/d2nr04350e

rsc.li/nanoscale

1. Introduction

Active control of heat transport at the nanoscale is vital for various applications, including thermal logic computing, thermal management, and energy conversion. One key component to realizing thermal control in solid-state devices is the thermal rectifier, which consists of two terminals and enables heat transport in preferential directions.[1] To evaluate its performance, a figure of merit termed thermal rectification factor (TRF) is defined as TRF = $(Q_f - Q_r)/Q_r$, where Q_f and Q_r denote the heat flux under the forward and reverse temperature bias, respectively. Thermal rectifiers with TRFs greater than ten are required for practical use,[2] but this value can hardly be achieved with conventional phonon-based thermal rectifiers. The reason is that their contact heat-conducting channels between the two terminals[3–6] suffer from limitations such as low group velocity of acoustic phonons, interfacial phonon scattering, and multiple phonon–phonon interactions.[7,8] In contrast, near-field radiative thermal rectifiers (NFRTRs), based on photon tunneling through non-contact terminals, can overcome these limitations to yield much higher efficiency and have gained growing popularity in recent years.

The TRF of a NFRTR is determined by the temperature-dependent electromagnetic (EM) properties of its terminal materials.[9] The basic requirement is that they should enable a spectral match to enhance the near-field radiative heat flux under a given forward temperature bias, while the spectral match should diminish due to their varied temperature dependence when the bias is reversed, thus strongly attenuating the heat flux. In this way, an asymmetry in heat flux between the forward and reverse scenarios is created and thus high TRFs can be achieved. To date, numerous NFRTRs by pairing dissimilar terminals among various polar dielectrics,[10,11] low-dimensional materials,[12,13] and phase change materials[14–17] have been explored. However, a contradiction in these designs is that these asymmetrical material pairings with mismatched EM properties significantly hinder the spectral match,[18,19] thereby limiting the radiative heat flux. Besides, the heat transport asymmetry in these systems remains weak due to the limited temperature dependence of the materials' EM properties. Although three-body systems have recently been proposed to strengthen this asymmetry by introducing many-body interactions, enabling thermal rectification even without temperature-dependent EM properties, the obtained TRFs remain low (~1).[20] Therefore, it is still a challenging task to design

[a]*CAS Key Laboratory of Nanophotonic Materials and Devices, CAS Key Laboratory of Standardization and Measurement for Nanotechnology, CAS Center for Excellence in Nanoscience, National Center for Nanoscience and Technology, Beijing 100190, China. E-mail: daiq@nanoctr.cn.nm*

[b]*Center of Materials Science and Optoelectronics Engineering, University of Chinese Academy of Sciences, Beijing 100049, China*

† Electronic supplementary information (ESI) available. See DOI: https://doi.org/10.1039/d2nr04350e

rational terminal pairings for NFRTRs to achieve TRFs higher than 100.

In the present study, a design scheme for NFRTRs is proposed to decouple the above-mentioned antithetical requirements for terminal materials by using distinct gap-isolated heterostructures, where a pair of layers supporting infrared (IR) polaritons are separately stacked on a thermally-expanding layer and a rigid substrate. The symmetrical polaritonic layers can provide stable near-field radiative channels for heat flux, while the thermally-expanding layer can modulate the gap size with flipped temperature bias to allow high contrasts in heat flux due to its sharp gap-size dependence.[18,21–23] A record-high TRF ($\sim 10^4$) has been achieved with the pairing of hBN/PDMS/SiO_2 and hBN/SiO_2 due to the thermally excited phonon polaritons, and it can be further boosted by the effective polaritonic coupling in graphene/hBN-based heterostructures. These TRFs have demonstrated an improvement of 1–4 orders of magnitude over previous studies (Table S1 in the ESI†), indicating the tremendous potential of the proposed scheme to design highly-efficient NFRTRs. It is quite impressive that this scheme depends on the spatial distributions of evanescent fields mediated by surface polaritons (SPs) across the vacuum gap rather than their spectral distributions, thus providing a rectification mechanism distinct from previous studies. Such a mechanism not only improves the performance of a photon-based thermal rectifier but also derives high design flexibility by taking advantage of enriched polaritons in 2D materials.

2. Methodology

2.1 Model systems

The proposed NFRTR design and its working principle are schematically illustrated in Fig. 1. The kernel in this design is the two distinct terminal heterostructures separated by a vacuum gap (d), where a pair of thin polaritonic layers are separately stacked on a thermally-expanding layer and a rigid substrate. Each heterostructure consists of at least two functional layers. As for the hot terminal heterostructure under the forward scenarios, the active layer with a large coefficient of thermal expansion (CTE) can modulate the gap size in response to the temperature changes, while the radiative layer supporting IR polaritons can provide near-field radiative channels for heat flux. More diverse configurations can be obtained by incorporating additional layers into each functional layer. Hence, this scheme is quite general due to its flexible modular designs.

Assuming that fixed constraints or other feasible measures are applied to the active terminal, directional thermal expansion/contraction and desired gap size variation can be obtained. In the forward scenarios (left panel in Fig. 1), the vacuum gap (d_f) decreases due to the downward movement of the hot terminal caused by the thermal expansion of the active layer, resulting in greatly enhanced heat flux. When the temperature bias is reversed (right panel in Fig. 1), the vacuum gap (d_r) enlarges due to the thermal contraction of the active layer, thus attenuating the heat flux.

In the following sections, specific material combinations are applied to implement this scheme and to demonstrate its thermal rectification potential.

2.2 Computational techniques

Within the theoretical framework of fluctuational electrodynamics,[24] the near-field radiative heat flux Q across the vacuum gap d between bi-planar heterostructures (Fig. 1) can be computed as

$$Q(T_h, T_c, d) = \frac{1}{4\pi^2}\int_0^\infty [\Theta(\omega, T_h) - \Theta(\omega, T_c)]\mathrm{d}\omega \int_0^\infty [\xi_s(\omega,\beta) + \xi_p(\omega,\beta)]\beta \mathrm{d}\beta, \quad (1)$$

where $\Theta(\omega,T) = \hbar\omega/[\exp(\hbar\omega/k_BT) - 1]$ is the mean energy of a Planck oscillator; ω is the angular frequency; β is the magnitude of the in-plane wavevector; T_h and T_c are the equilibrated temperatures of the two terminals; and $\xi(\omega,\beta)$ is the energy

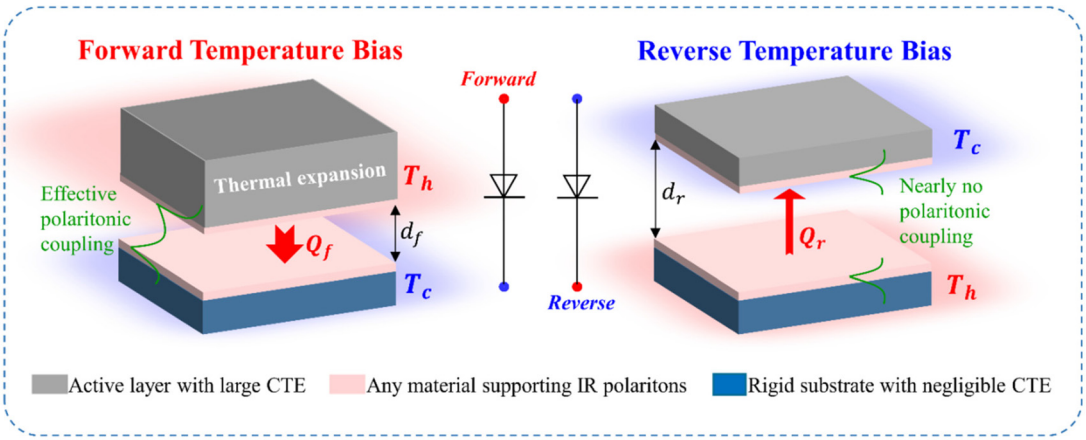

Fig. 1 Schematic illustration of the proposed NFRTR design and its working principle.

transmission coefficient for s- and p-polarized waves, which is also termed the photon tunneling probability (PTP) and given as

$$\xi_{n=\mathrm{s,p}}^{1,2}(\omega,\beta)=\begin{cases}\dfrac{(1-|R_{\mathrm{n}}^{1}|^{2})(1-|R_{\mathrm{n}}^{2}|^{2})}{\left|1-R_{\mathrm{n}}^{1}R_{\mathrm{n}}^{2}e^{-2ik_{z0}d}\right|^{2}}, & \beta\le k_0\\ \dfrac{4\mathrm{Im}(R_{\mathrm{n}}^{1})\mathrm{Im}(R_{\mathrm{n}}^{2})e^{-2|k_{z0}|d}}{\left|1-R_{\mathrm{n}}^{1}R_{\mathrm{n}}^{2}\mathrm{e}^{-2ik_{z0}d}\right|^{2}}, & \beta>k_0\end{cases} \quad (2)$$

where the superscripts 1 and 2 denote the emitter and receiver, respectively; $k_0 = \omega/c$ is the vacuum wavevector; k_{z0} is the out-of-plane wavevector given by $k_{z0} = (k_0{}^2 - \beta^2)^{1/2}$; and R_{n} is the Fresnel reflection coefficient of each terminal heterostructure, which can be derived for multilayers by using the scattering matrix method.[25,26] In eqn (2), the far-field ($\beta \le k_0$, propagating modes) contribution to the heat flux is clearly separated from the near-field ($\beta > k_0$, evanescent modes) one. Due to the exponential damping of evanescent modes, β is limited at a given frequency to a value below the cutoff wavevector k_{c}.[27,28] More details about this calculation can be found in the ESI.†

2.3 Materials properties

2.3.1 Thermally expanding materials. Thermal expansion is a material's tendency to change its volume in response to temperature variation. When a material is heated, the kinetic energy of molecules increases, causing them to move more and, in most cases, maintain a greater average separation. It is an intrinsic property of a material that can be quantified using the coefficient of thermal expansion (CTE). The required linear CTE can be calculated as

$$\alpha=\frac{1}{L}\frac{\mathrm{d}L}{\mathrm{d}T}(\mathrm{K}^{-1}), \quad (3)$$

where L is the linear dimension (length or thickness) and $\frac{\mathrm{d}L}{\mathrm{d}T}$ is the change rate of the linear dimension per unit change in temperature. Polymers have much higher CTEs than inorganic materials and can expand to a greater extent when heated to the same temperature.

Here, polydimethylsiloxane (PDMS) and silica are selected as the active layer and the rigid substrate, respectively. PDMS is a silicone polymer commonly used in biomedical, microfluidic, or lab-on-a-chip applications due to its low cost, rapid manufacturing, and ease of use.[29] Furthermore, it has high thermal sensitivity and thus has been widely used in photothermal actuators.[30,31] The CTE of PDMS is reported as a constant, ranging from 2.66×10^{-4} to 3.14×10^{-4} (K^{-1}), and it works normally in the temperature range from −45 °C to 200 °C.[32–34] Thus, the CTE of PDMS is set constant as 3×10^{-4} K^{-1} and the operating temperature range (T_{h}) is considered as 300–500 K in this study. Notably, if other high-CTE materials with higher-temperature stability are selected, the operating temperature of the designed NFRTRs can be accordingly expanded to higher values. For a given thickness of the PDMS layer (t_{PDMS}) under a given temperature gradient (ΔT), the thermally-induced gap size variation can be determined as follows:

$$\Delta d=\alpha t_{\mathrm{PDMS}} \quad \Delta T=\alpha t_{\mathrm{PDMS}}(T_{\mathrm{h}}-T_{\mathrm{c}}). \quad (4)$$

This means that a gap size reduction of 300 nm can be achieved for a 20 μm-thick PDMS layer with a temperature rise of 50 K. Obviously, larger gap size variations can be obtained by using thicker PDMS layers or larger temperature gradients. In contrast, silica possesses a CTE of about 5×10^{-7} K^{-1}, which causes negligible gap size variations under the same conditions.

2.3.2 Two-dimensional (2D) materials supporting infrared polaritons. In principle, any material enabling enhanced near-field radiative heat transfer can be selected as the radiative layer. Materials supporting IR polariton modes outperform those based on evanescent frustrated modes in this respect due to their more pronounced enhancement and better tunability.[22] Herein, 2D van der Waals materials including graphene and hexagonal boron nitride (hBN) are chosen due to their advantages such as single-atom-layer thickness, broadband IR frequency responses, strong field localization in 2D, and highly tunable polaritonic modes. All these advantages make them well-suited for mediating, enhancing, and tailoring near-field radiative heat transfer. Previous research has demonstrated their potential in this regard.[35]

The dielectric function of graphene with a finite thickness of h can be given as[36]

$$\varepsilon(\omega,h)=1+\frac{i\sigma(\omega)}{\varepsilon_0\omega h}, \quad (4)$$

where ε_0 is the vacuum permittivity, ω is the angular frequency, and σ is its in-plane conductivity, which can be approximated at room temperature T ($k_{\mathrm{B}}T \ll E_{\mathrm{F}}$) as[35]

$$\sigma=\frac{ie^2E_{\mathrm{F}}}{\pi\hbar^2(\omega+i\tau^{-1})}+i\frac{e^2}{4\pi\hbar}\ln\left[\frac{2|E_{\mathrm{F}}-\hbar(\omega+i\tau^{-1})}{2|E_{\mathrm{F}}|+\hbar(\omega+i\tau^{-1})}\right], \quad (5)$$

where $\tau = \mu_{\mathrm{cm}}E_{\mathrm{F}}/ev_{\mathrm{F}}{}^2$ is the relaxation time; μ_{cm} is the carrier mobility; and E_{F} and $v_{\mathrm{F}} = 10^6$ m s^{-1} are the Fermi energy and velocity, respectively. Unless otherwise specified, the parameters for the graphene monolayer used in this study are h = 0.334 nm, $\mu_{\mathrm{cm}} \approx 2000$ cm^2 V^{-1} s^{-1}, and E_{F} = 0.3 eV.

hBN is a natural hyperbolic material supporting hyperbolic phonon polaritons (HPhPs) within two reststrahlen bands (RBs), enclosed by transverse-optical (TO) and longitudinal-optical (LO) phonon frequencies. Two types of HPhPs can be excited in the hBN crystal layer (type I: $\varepsilon_\perp > 0$, $\varepsilon_\parallel < 0$ and type II: $\varepsilon_\perp < 0$, $\varepsilon_\parallel > 0$) in the RBs, characterized by a negative real part of the dielectric constant. The in-plane and out-of-plane dielectric constants of hBN can be well approximated by the classic Lorentz model as follows:

$$\varepsilon_{\mathrm{hBN,m}}=\varepsilon_{\infty,\mathrm{m}}\left[1+\frac{(\omega_{\mathrm{LO,m}})^2-(\omega_{\mathrm{TO,m}})^2}{(\omega_{\mathrm{TO,m}})^2-\omega^2-i\omega\Gamma_{\mathrm{m}}}\right], \quad (6)$$

where the subscript $m = \perp$ or $\parallel$ denotes the in-plane and out-of-plane components corresponding to the perpendicular or

parallel direction to the optical axis of the hBN crystal, respectively; $\varepsilon_{\infty,m}$ is the high-frequency permittivity; $\omega_{LO,m}$ and $\omega_{TO,m}$ are the LO and TO phonon frequencies, respectively; and Γ_m is the damping factor. Here the fitting parameters are given as[37,38] $\varepsilon_{\parallel,\infty} = 2.8$, $\omega_{LO,\parallel} = 845\ cm^{-1}$, $\omega_{TO,\parallel} = 785\ cm^{-1}$, and $\Gamma_\parallel = 1\ cm^{-1}$, while $\varepsilon_{\perp,\infty} = 3$, $\omega_{LO,\perp} = 1630\ cm^{-1}$, $\omega_{TO,\perp} = 1395\ cm^{-1}$, and $\Gamma_\perp = 2\ cm^{-1}$. For all calculations, the hBN thickness is fixed at 20 nm. The dielectric functions of PDMS and silica can be found in the literature.[39] The dielectric constants of the four adopted materials have been plotted as a function of angular frequency, as shown in Fig. S2 in the ESI.†

3. Results and discussion

3.1 Gigantic TRFs and underlying mechanisms

We now demonstrate that ultrahigh TRFs can be accomplished in the NFRTR designs with gap size variations induced by thermal expansion/contraction of the PDMS layer. As an illustration, we set $T_c = 300$ K and a tunable T_h to achieve the required gap size variations (eqn (4)). It has been well established that heat transport is in the crossover regime between conduction and radiation when the gap size is down to a few nanometers.[40,41] To avoid any possible impacts from thermal conduction, the gap size under the forward bias d_f, *i.e.*, the minimum operating gap size, is fixed at 10 nm to serve as the benchmark. The reverse gap size can be accordingly determined using $d_r = d_f + \Delta d$. In the following calculations, t_{PDMS} is fixed at 20 μm, and a 1 mm-thick silica substrate is added beneath both terminal heterostructures to provide the necessary support. Notably, both terminals work at equilibrated temperatures of T_h and T_c, respectively, implying that heat transfer inside them is not taken into account.

As shown in Fig. 2a, both greatly enhanced Q and ultrahigh TRFs have been achieved even with small temperature gradients for the two distinct NFRTR designs, *i.e.* hBN- and graphene/hBN-based pairings. For the former design, a heat flux of 4257.15 W m^{-2}, about 692 times higher than that of the blackbody radiation limit (6.15 W m^{-2}), is achieved under a forward bias of only 1 K. Then it surges with elevated temperature gradients (Fig. 2a) since more phonon modes are excited at higher temperatures. This intensive heat transfer is mainly attributed to the contribution of evanescent waves mediated by the cavity phonon polariton modes thermally excited between the bi-planar paring of hBN/PDMS/SiO_2 and hBN/SiO_2. Two main sharp peaks centered at ~1.6×10^{14} rad s^{-1} and ~2.8×10^{14} rad s^{-1} (Fig. 2b), corresponding to the energies of HPhPs within two RBs of the hBN layer, dominate the spectral heat flux, together with two other small peaks mediated by the optical phonon energies of SiO_2 (Fig. S2 in the ESI†). When the temperature bias is reversed and increases from −1 K to −200 K, the heat flux Q considerably decreases at first due to the enlarged gap size and then gradually increases due to the increased temperature gradients (Fig. 2a). The reason for the former behavior is that the SP-mediated evanescent modes decay exponentially in the vacuum gap, leading to a

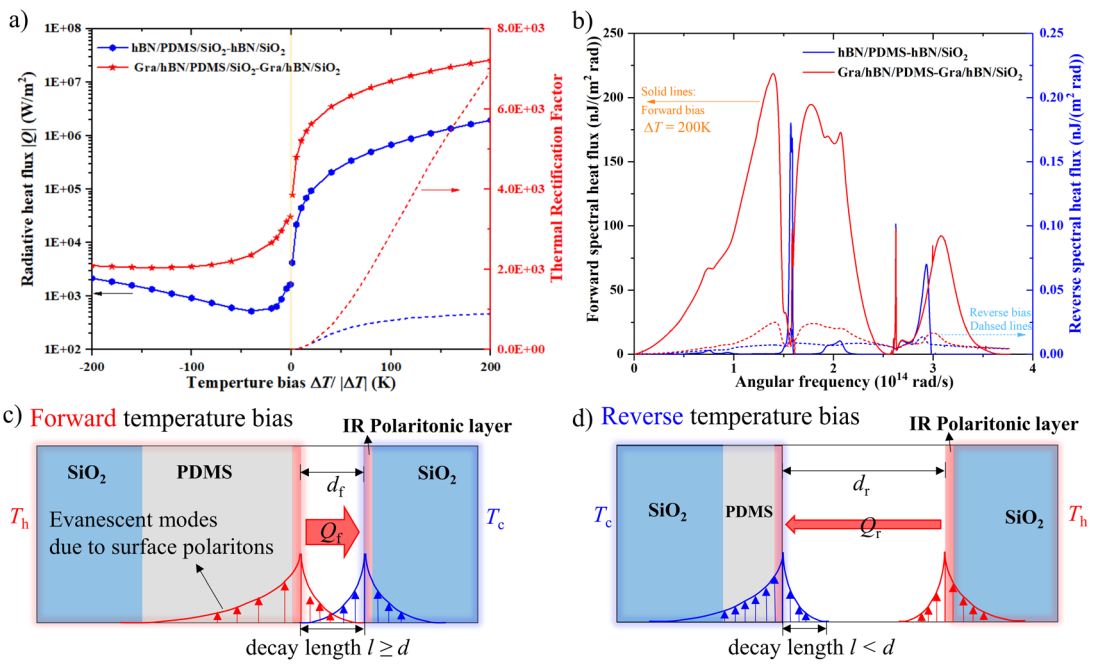

Fig. 2 Thermal rectification performance of NFRTRs with hBN- and graphene/hBN-based parings, together with the underlying mechanisms. (a) Radiative heat flux (solid lines with markers) and TRFs (dashed lines) as a function of temperature bias ΔT. Note that the TRF characterizes the relative enhancement of Q between the forward ($+\Delta T$) and reverse ($-\Delta T$) scenarios under the same absolute temperature difference ($|\Delta T|$). Thus TRFs are plotted as a function of $|\Delta T|$. (b) Spectral heat flux under both forward and reverse biases of 200 K, corresponding to forward and reverse gap sizes of 10 nm and 1210 nm. (c and d) Schematic illustration of the underlying mechanisms for the proposed NFRTR designs under (c) forward and (d) reverse bias conditions.

considerable decrease in the number of available surface modes with increasing gap size. More specifically, only SP modes with the decay length l approximately equal to or larger than the gap size ($l \geq d$) can be tunneled across the gap,[22] thus contributing to the Q enhancement. This naturally happens when the forward gap size is 10 nm. In contrast, nearly no SP modes can be tunneled when the reverse gap size enlarges and exceeds the decay length ($l < d$), resulting in a considerable decrease in Q. This trend has been well elucidated by the profile of the reverse spectral heat flux (Fig. 2b), which closely resembles that of the forward one but has an amplitude being more than 10^3 lower. In this way, a strong asymmetry in heat fluxes is created between the forward and reverse scenarios, thus achieving high TRFs. For this hBN-based NFRTR, a maximal TRF of ~900 is obtained under $|\Delta T|$ = 200 K. As schematically illustrated in Fig. 2c and d, these high TRFs originate from the contrasted spatial distributions of the SP-mediated evanescent fields between the forward and reverse scenarios, rather than their spectral distributions, thus providing a rectification mechanism that differs from the previous studies.

The performance of NFRTRs can be further improved by symmetrically stacking a graphene monolayer on the radiative layer of the original heterostructure. The heat flux for this graphene/hBN-based NFRTR is about 25.98 MW m^{-2} under a forward bias of 200 K, which is about 13.25 times higher than that of the hBN-based design. This significant enhancement is attributed to the effective coupling of SPPs in graphene and SPhPs in both hBN and SiO_2, which forms the hybridized polaritonic modes enabling a more broadband spectral heat flux (the red solid line in Fig. 2b). The underlying mechanism can be further elucidated using the PTP contour maps in Fig. 3. Notably, to better illustrate the roles played by the SPs, Fig. 3a–d show the PTP mediated by the SP modes only, *i.e.*, $\xi_p(\omega,\beta)$ is calculated over $k_0 < \beta < k_c$. Two distinct features can be observed. First, the PTP bands in Fig. 3b appear both broader and brighter than their counterparts in Fig. 3a, indicating the heat transfer enhancement mediated by the effective polaritonic coupling in the graphene/hBN-based design. Second, the PTP bands under the reverse bias significantly decay in large wavevectors β, and become invisible for $\beta > 8 \times 10^7$ m^{-1} (Fig. 3c and d). The reason lies in that the decay length l of SP modes is approximately equal to the inverse of the momentum (wavevector β), *i.e.*, $l = 1/\beta$,[22] indicating that SP modes with larger β have smaller l and thus lead to faster

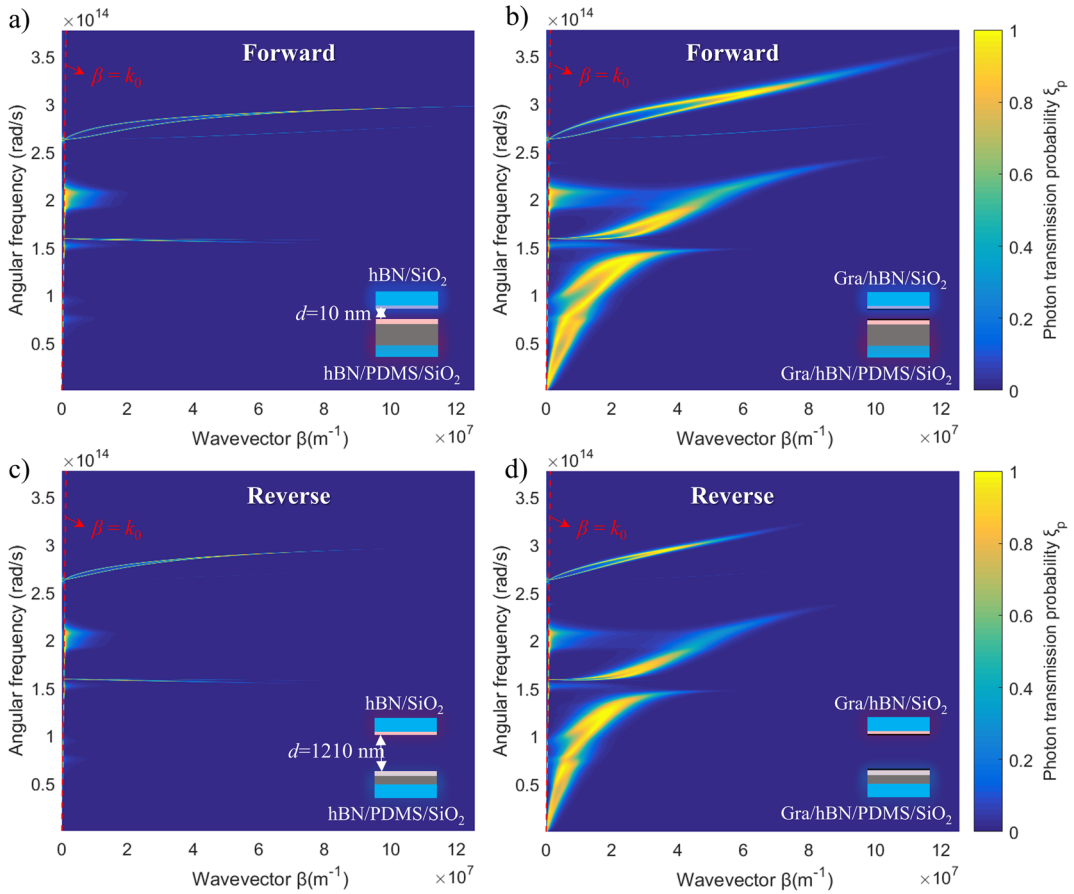

Fig. 3 Contour maps displaying the PTP of p-polarized SP modes thermally excited between distinct pairings: (a) hBN/PDMS/SiO_2-hBN/SiO_2 and (b) graphene/hBN/PDMS/SiO_2-graphene/hBN/SiO_2 under a forward temperature bias of 200 K and a gap size of 10 nm. (c and d) Corresponding PTP contour maps under the same reverse bias with a corresponding gap size of 1210 nm. The red dashed lines illustrate the vacuum light line.

decays. Besides, the cutoff wavevector k_c, *i.e.*, the upper limit of β for the contributing modes, is inversely proportional to the gap size $k_c \cong 1/d$.[27,28,42] The reverse gap size is 1210 nm in these cases, leading to a greatly reduced k_c and also the contributing mode numbers compared with those in the forward cases. This also explains the trend of its reverse heat flux which gradually decreases and then saturates as ΔT changes from −1 K to −200 K (Fig. 2a). More hybridized polaritonic modes with large β in the graphene/hBN-based design decay with increasing d compared to the case of the hBN-based design (Fig. 3), thus leading to a faster decrease of Q. This difference eventually results in a much higher contrast of Q for the graphene–hBN design, *e.g.* with a TRF of ~6936 achieved under a 200 K temperature bias, which is 7.7 times that of the counterpart of the hBN-based one (Fig. 2a). These TRFs can be further optimized by tailoring the chemical potential of the monolayer graphene and the hBN thickness, as shown in Fig. S4 in the ESI.†

3.2 Unlimited potentials due to high tunability and design flexibility

To further demonstrate the rectification potential of the proposed scheme, we computed the Q for the above-mentioned two pairings with d ranging from 10 nm to 1 μm under both ΔT of 20 K and 100 K. Near-field heat transfer occurs through the evanescent coupling of thermally excited surface resonances, thus making Q scale inversely with the gap size d.[23] Here, a power-law model $Q = \gamma d^n$ ($n < 0$) is used to determine their quantitative relationship, where the exponent n is a geometry-dependent factor and γ is the fitting coefficient.[23]

As shown in Fig. 4a and c, fitting curves indicate a near-perfect d^{-2} scaling relationship of Q for all cases, which is consistent with previous studies for similar parallel-plane configurations.[23,28,43–45] This dependence signifies the strong contribution of surface modes (*i.e.*, SPPs in graphene, SPhPs in hBN and SiO_2, and their hybridized modes) in the near-field radiative heat transfer. Detailed fitting parameters can be found in Fig. S6 of the ESI.† This relationship also provides an intuitive understanding of the sharp gap-size dependence of the radiative heat flux, as well as an optimistic upper bound for the gap-size variation-induced thermal rectification. As indicated by the different γ values, the two pairings exhibit different d-dependences of Q. The NFRTR based on the graphene/hBN heterostructure exhibits a much stronger dependence than the hBN-based one, due to the effective coupling of SPPs and SPhPs in the combination of polar dielectrics with

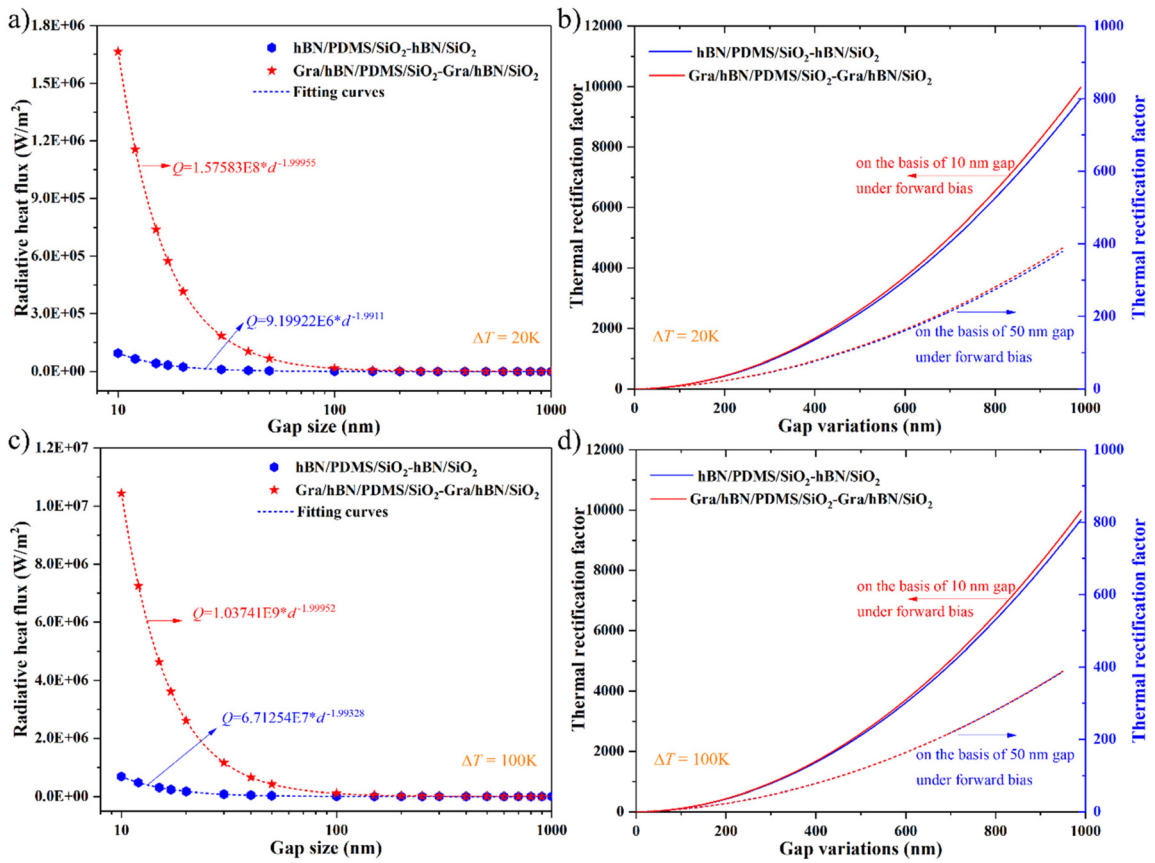

Fig. 4 Gap-size dependence of near-field radiative heat flux for hBN- and graphene/hBN-based pairings under constant temperature biases of (a) 20 K and (c) 100 K, together with the corresponding power-law fitting curves. TRFs as a function of gap size variations for both designs under the same temperature biases of (b) 20 K and (d) 100 K.

IR plasmonic materials. This combination finally results in higher TRFs, particularly with larger gap size variations. Record-high TRFs of ~9597 and ~9980 have been obtained for the hBN- and graphene/hBN-based designs under d_f = 10 nm, d_r = 1000 nm, and ΔT = 20 K, respectively. Furthermore, these TRFs remain nearly unchanged for both designs when ΔT increases from 20 K to 100 K (Fig. 4b and d), even though the amplitude of Q increases significantly (Fig. 4).

TRFs achieved for NFRTRs in this work have been compared with those in previous publications, as listed in Table S1 (ESI).† An improvement of 1–4 orders of magnitude has been achieved, indicating the tremendous potential of the proposed scheme for designing highly-efficient NFRTRs. Here we would like to emphasize that the key to achieving ultra-high TRFs in our proposed design scheme for NFRTRs is to obtain a strong gap-size dependence of the radiative heat flux. Specifically, measures that enable the further enhancement of the forward heat flux but the rapid decay of the reverse heat flux with increasing gap size would help to improve the TRFs. Hence, we anticipate that other IR polaritonic materials such as α-MoO_3 and BP,[46,47] and elaborate nanostructures such as multilayers and *meta*-surfaces,[48,49] particularly those featuring hyperbolic properties with broadband responses and large transverse wavevectors, can serve as alternative radiative layers to achieve extra gains. Besides, both the active layer and the substrate can be appropriately selected and matched with the radiative layers for further optimization. When it comes to the experimental implementation of this NFRTR concept, challenges have to be tackled such as maintaining the surface parallelism alignment under dynamic variations of the gap size at the nanoscale, avoiding undesired deformation of the heterostructures induced by temperature changes, and optimizing the active layer (*e.g.*, the CTE and thickness) to compromise between the available gap size variations and the compactness requirement of related devices.

It should be mentioned that the corresponding TRFs for both designs decrease more than 20 times as the forward gap size increases from 10 nm to 50 nm, with the maximum TRFs decreasing to ~400 (Fig. 4b and d), due to the rapid decay of the SP modes with increasing gap size. However, these TRFs are still much higher than those achieved in most of the previously reported NFRTRs (Table S1 in the ESI†). More importantly, the proposed scheme offers higher design flexibility and is much simpler to implement in experiments. The design flexibility of this scheme, as well as the achievable superior performance, has also been demonstrated by replacing the radiative layer with traditional polar dielectrics such as SiO_2 and SiC, as discussed in section S5 in the ESI.†

4. Conclusions

In summary, we have proposed a novel scheme to design NFRTRs by stacking a pair of polaritonic layers separately on a thermally-expanding layer and a rigid substrate. In this scheme, the symmetrical polaritonic layers provide stable radiative channels for heat flux, while the thermally-expanding layer can modulate the gap size with flipped temperature biases to allow high contrasts in heat flux. This scheme relies on the spatial distributions of SP-mediated evanescent fields, which decay exponentially with increasing gap size. The hBN-based paring has been demonstrated to yield a record-high TRF of ~10^4 due to the thermally excited phonon polaritons, which can be further boosted by the polaritonic hybridizations in the graphene/hBN-based heterostructures. This study paves the way to introduce more radiative material candidates for NFRTRs with high efficiency, thus opening new avenues for their long-awaited experimental realization.

Conflicts of interest

There are no conflicts to declare.

Acknowledgements

The authors greatly acknowledge the financial support from the National Natural Science Foundation of China (Grant No. 51925203), the Strategic Priority Research Program of the Chinese Academy of Sciences (Grant No. XDB36000000), and the Special Research Assistant Program of the Chinese Academy of Sciences.

References

1 N. Li, J. Ren, L. Wang, G. Zhang, P. Hänggi and B. Li, *Rev. Mod. Phys.*, 2012, **84**, 1045–1066.
2 M. J. Martínez-Pérez, A. Fornieri and F. Giazotto, *Nat. Nanotechnol.*, 2015, **10**, 303–307.
3 H. Wang, S. Hu, K. Takahashi, X. Zhang, H. Takamatsu and J. Chen, *Nat. Commun.*, 2017, **8**, 1–8.
4 M. Kasprzak, M. Sledzinska, K. Zaleski, I. Iatsunskyi, F. Alzina, S. Volz, C. M. Sotomayor Torres and B. Graczykowski, *Nano Energy*, 2020, **78**, 105261.
5 C. W. Chang, D. Okawa, A. Majumdar and A. Zettl, *Science*, 2006, **314**, 1121–1124.
6 J. Zhao, D. Wei, A. Gao, H. Dong, Y. Bao, Y. Jiang and D. Liu, *Appl. Therm. Eng.*, 2020, **176**, 115410.
7 P. Ben-Abdallah and S. A. Biehs, *Phys. Rev. Lett.*, 2014, **112**, 1–5.
8 A. Ghanekar, J. Ji and Y. Zheng, *Appl. Phys. Lett.*, 2016, **109**, 123106.
9 Y. Li, W. Li, T. Han, X. Zheng, J. Li, B. Li, S. Fan and C. W. Qiu, *Nat. Rev. Mater.*, 2021, **6**, 488–507.
10 C. R. Otey, W. T. Lau and S. Fan, *Phys. Rev. Lett.*, 2010, **104**, 1–4.
11 K. Joulain, Y. Ezzahri, J. Drevillon, B. Rousseau and D. De Sousa Meneses, *Opt. Express*, 2015, **23**, A1388–A1397.
12 G. Xu, J. Sun, H. Mao and T. Pan, *J. Quant. Spectrosc. Radiat. Transfer*, 2018, **220**, 140–147.

13 D. Feng, S. K. Yee and Z. M. Zhang, *Appl. Phys. Lett.*, 2021, **119**, 181111.
14 Y. Yang, S. Basu and L. Wang, *Appl. Phys. Lett.*, 2013, **103**, 163101.
15 A. Fiorino, D. Thompson, L. Zhu, R. Mittapally, S. A. Biehs, O. Bezencenet, N. El-Bondry, S. Bansropun, P. Ben-Abdallah, E. Meyhofer and P. Reddy, *ACS Nano*, 2018, **12**, 5174–5179.
16 Y. Liu, Y. Tian, F. Chen, A. Caratenuto, X. Liu, M. Antezza and Y. Zheng, *Appl. Phys. Lett.*, 2021, **119**, 123101.
17 Q. Li, H. He, Q. Chen and B. Song, *Phys. Rev. Appl.*, 2021, **16**, 014069.
18 B. Song, D. Thompson, A. Fiorino, Y. Ganjeh, P. Reddy and E. Meyhofer, *Nat. Nanotechnol.*, 2016, **11**, 509–514.
19 L. Tang, J. Desutter and M. Francoeur, *ACS Photonics*, 2020, **7**, 1304–1311.
20 I. Latella, P. Ben-Abdallah and M. Nikbakht, *Phys. Rev. B*, 2021, **104**, 1–8.
21 K. Kim, B. Song, V. Fernández-Hurtado, W. Lee, W. Jeong, L. Cui, D. Thompson, J. Feist, M. T. H. Reid, F. J. García-Vidal, J. C. Cuevas, E. Meyhofer and P. Reddy, *Nature*, 2015, **528**, 387–391.
22 M. Francoeur, *Nat. Nanotechnol.*, 2015, **10**, 206–208.
23 R. St-Gelais, L. Zhu, S. Fan and M. Lipson, *Nat. Nanotechnol.*, 2016, **11**, 515–519.
24 M. R. Sergei, A. K. Yurii and I. T. Valeryan, *Principles of Statistical Radiophysics*, Springer, New York, 1989.
25 S. Dai, Z. Fei, Q. Ma, A. S. Rodin, M. Wagner, A. S. McLeod, M. K. Liu, W. Gannett, W. Regan, K. Watanabe, T. Taniguchi, M. Thiemens, G. Dominguez, A. H. Castro Neto, A. Zettl, F. Keilmann, P. Jarillo-Herrero, M. M. Fogler and D. N. Basov, *Science*, 2014, **343**, 1125–1129.
26 B. Song, Y. Ganjeh, S. Sadat, D. Thompson, A. Fiorino, V. Fernández-Hurtado, J. Feist, F. J. Garcia-Vidal, J. C. Cuevas, P. Reddy and E. Meyhofer, *Nat. Nanotechnol.*, 2015, **10**, 253–258.
27 P. Ben-Abdallah and K. Joulain, *Phys. Rev. B: Condens. Matter Mater. Phys.*, 2010, **82**, 1–4.
28 S. A. Biehs, E. Rousseau and J. J. Greffet, *Phys. Rev. Lett.*, 2010, **105**, 3–6.
29 A. Kausar, *Polym.-Plast. Technol. Mater.*, 2020, **59**, 1148–1166.
30 Y. Hu, J. Liu, L. Chang, L. Yang, A. Xu, K. Qi, P. Lu, G. Wu, W. Chen and Y. Wu, *Adv. Funct. Mater.*, 2017, **27**, 1704388.
31 Y. Yang, Y. Liu and Y. Shen, *Adv. Funct. Mater.*, 2020, **30**, 1–7.
32 T. I. Lee, M. S. Kim and T. S. Kim, *Polym. Test.*, 2016, **51**, 181–189.
33 Y. H. Lin, S. W. Kang and T. Y. Wu, *Appl. Therm. Eng.*, 2009, **29**, 573–580.
34 N. Bowden, W. T. S. Huck, K. E. Paul and G. M. Whitesides, *Appl. Phys. Lett.*, 1999, **75**, 2557–2559.
35 B. Yang, D. Pan, X. Guo, H. Hu and Q. Dai, *Int. J. Therm. Sci.*, 2022, **176**, 107493.
36 A. Vakil and N. Engheta, *Science*, 2011, **332**, 1291–1294.
37 P. Li, I. Dolado, F. J. Alfaro-Mozaz, F. Casanova, L. E. Hueso, S. Liu, J. H. Edgar, A. Y. Nikitin, S. Vélez and R. Hillenbrand, *Science*, 2018, **359**, 892–896.
38 Z. Yuan, R. Chen, P. Li, A. Y. Nikitin, R. Hillenbrand and X. Zhang, *ACS Photonics*, 2020, **7**, 2610–2617.
39 E. D. Palik, *Handbook of Optical Constants of Solids*, Academic P., San Diego, USA, 1998.
40 V. Chiloyan, J. Garg, K. Esfarjani and G. Chen, *Nat. Commun.*, 2015, **6**, 6755.
41 K. Kloppstech, N. Könne, S. A. Biehs, A. W. Rodriguez, L. Worbes, D. Hellmann and A. Kittel, *Nat. Commun.*, 2017, **8**, 1–6.
42 S. A. Biehs, M. Tschikin and P. Ben-Abdallah, *Phys. Rev. Lett.*, 2012, **109**, 1–5.
43 J. B. Pendry, *J. Phys.: Condens. Matter*, 1999, **11**, 6621–6633.
44 J.-P. Mulet, K. Joulain, R. Carminati and J.-J. Greffet, *Microscale Thermophys. Eng.*, 2002, **6**, 209–222.
45 M. Ghashami, H. Geng, T. Kim, N. Iacopino, S. K. Cho and K. Park, *Phys. Rev. Lett.*, 2018, **120**, 175901.
46 W. Ma, P. Alonso-González, S. Li, A. Y. Nikitin, J. Yuan, J. Martín-Sánchez, J. Taboada-Gutiérrez, I. Amenabar, P. Li, S. Vélez, C. Tollan, Z. Dai, Y. Zhang, S. Sriram, K. Kalantar-Zadeh, S. T. Lee, R. Hillenbrand and Q. Bao, *Nature*, 2018, **562**, 557–562.
47 D. Correas-Serrano, A. Alù and J. S. Gomez-Diaz, *Phys. Rev. B*, 2017, **96**, 1–9.
48 B. Zhao, B. Guizal, Z. M. Zhang, S. Fan and M. Antezza, *Phys. Rev. B*, 2017, **95**, 1–9.
49 V. Fernández-Hurtado, F. J. García-Vidal, S. Fan and J. C. Cuevas, *Phys. Rev. Lett.*, 2017, **118**, 1–6.